THE JOURNAL OF PHYSICAL CHEMISTRY LETTERS
A JOURNAL OF THE AMERICAN CHEMICAL SOCIETY

pubs.acs.org/JPCL

Letter

Ag–Bi Charge Redistribution Creates Deep Traps in Defective $Cs_2AgBiBr_6$: Machine Learning Analysis of Density Functional Theory

Dongyu Liu, Carlos Mora Perez, Andrey S. Vasenko,* and Oleg V. Prezhdo*

Cite This: *J. Phys. Chem. Lett.* 2022, 13, 3645–3651

Read Online

ACCESS | Metrics & More | Article Recommendations | Supporting Information

ABSTRACT: Lead-free double perovskites hold promise for stable and environmentally benign solar cells; however, they exhibit low efficiencies because defects act as charge recombination centers. Identifying trap-assisted loss mechanisms and developing defect passivation strategies constitute an urgent goal. Applying unsupervised machine learning to density functional theory and nonadiabatic molecular dynamics, we demonstrate that negatively charged Br vacancies in $Cs_2AgBiBr_6$ create deep hole traps through charge redistribution between the adjacent Ag and Bi atoms. Vacancy electrons are first accepted by Bi and then shared with Ag, as the trap transforms from shallow to deep. Subsequent charge losses are promoted by Ag and Bi motions perpendicular to rather than along the Ag–Bi axis, as can be expected. In contrast, charge recombination in pristine $Cs_2AgBiBr_6$ correlates most with displacements of Cs atoms and Br–Br–Br angles. Doping with In to replace Ag at the vacancy maintains the electrons at Bi and keeps the trap shallow.

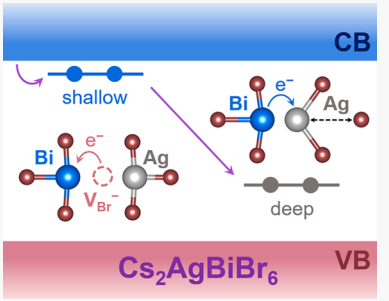

Metal halide perovskites are potential candidates for the next-generation solar cells with excellent optoelectronic properties,[1] which have enabled the rapid increase of power conversion efficiency (PCE) from 3.8% in 2009 to over 25% since 2021.[2−4] However, the presence of toxic lead is essential for achieving such high PCE because of its unique role in the perovskite lattice.[5,6] Replacing lead with the same group element tin is a feasible approach to eliminate the toxicity, but the produced Sn^{2+} species will raise the oxidative instability issue.[7,8] Recently, the $Cs_2AgBiBr_6$ double perovskite has emerged as a promising solution for constructing a stable and lead-free perovskite. $Cs_2AgBiBr_6$ combines Ag^+ and Bi^{3+} ions to replace two Pb^{2+} ions.[9−11] Single-crystal studies indicate that the charge carriers have a long lifetime and a large diffusion length,[12,13] which implies that $Cs_2AgBiBr_6$ may have good photovoltaic performance.[14] Nevertheless, its PCE is only around 3% at present because of various defects,[15−17] which strongly motives the exploration for reducing the energy losses.

Typically, defects would induce midgap trap states that obstruct carrier transport and lead to trap-assisted nonradiative recombination, which dissipate the electrical energy as heat.[18] Experimental works have identified these detrimental defects in $Cs_2AgBiBr_6$ and developed strategies to passivate them.[19−22] However, the lack of explicit knowledge of correlations between defect configurations and relevant trap states limits the investigation efficiency.[23] Recently, machine learning (ML) analysis of nonadiabatic molecular dynamics (NA-MD) simulations has emerged as a powerful approach to uncover the interdependence between the structural and electronic properties and excited-state dynamics.[24−33] The energy gap and nonadiabatic coupling (NAC) fluctuations have been found dominated by structural deformations[34,35] and chemical environment of individual elements,[36,37] rather than particular atomic motions, allowing one to uncover defect features that are key in producing trap-assisted recombination centers. Such analyses provide direct guidelines on eliminating the detrimental traps.

In this work, we use unsupervised ML, in conjunction with density functional theory (DFT) and NA-MD calculations, to investigate the recombination centers in defective $Cs_2AgBiBr_6$ induced by the negatively charged Br vacancies (V_{Br}^-). The species is analogous to the negatively charged Bi dopant in $MAPbBr_3$, where the reduced $BiBr_6$ octahedra distort and produce deep trap states.[38,39] However, we demonstrate that a charge redistribution rather than a structural distortion is the origin of the deep defect state in the $Cs_2AgBiBr_6$ double perovskite. The electronic structure analysis indicates that the electrons from the vacancies are first accepted by Bi^{3+} and then are shared with Ag^+, as the Ag–Bi distance shortens. The stabilization mediated by the charge sharing causes the trap level to move downward in energy from shallow to deep. Surprisingly, although the defect states originate from the interaction between Ag and Bi, ML analysis shows that neither the energy gaps nor the NACs have strong correlations with the Ag–Bi distance. In contrast, these electronic properties are

Received: March 25, 2022
Accepted: April 15, 2022
Published: April 18, 2022

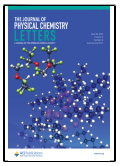

https://doi.org/10.1021/acs.jpclett.2c00869
J. Phys. Chem. Lett. 2022, 13, 3645–3651

governed by the individual motions of Ag and Bi perpendicular to the Ag−Bi axis. The bandgap and NAC in pristine $Cs_2AgBiBr_6$ correlate most strongly with Cs atom displacement and Br−Br−Br angle, even though Cs does not contribute to the relevant electronic states. Doping with the less electrophilic In to replace Ag at the vacancy suppresses the charge transfer from Bi and keeps the defect state shallow. The reported results provide new insights into understanding the defects in double perovskites and assist in developing improved optoelectronic materials.

The periodic DFT calculations were performed with the Vienna Ab initio Simulation Package (VASP).[40−43] The Perdew−Burke−Ernzerhof (PBE) functional[44] and the projected-augmented wave (PAW) method[45,46] were used to describe the electron−ion interactions. The cutoff energy of the plane wave basis was set as 450 eV. The convergence criteria for the energy and geometry optimization calculations were 10^{-5} eV and 0.01 eV/Å, respectively. The $Cs_2AgBiBr_6$ bulk was modeled with a $1 \times 1 \times 2$ supercell containing 80 atoms and a $3 \times 3 \times 1$ k-point grid. The optimized structures were then thermalized at 300 K in canonical molecular dynamics (MD) simulations for 10 ps with the time step of 1 fs, and the trajectories of the last 4 ps were selected to calculate the NA-MD Hamiltonian. The structures were visualized with the VESTA software package.[47]

The NACs characterize dependence of the electronic wave functions on atomic motions. They generate off-diagonal elements of the many-electron Hamiltonian that is used in the time-dependent Schrödinger equation.[48−54] A large NAC value indicates a strong coupling between two electronic states and a high probability of a nonradiative transition between the states. In the current simulations, the NACs are numerically calculated from the overlap between two wave functions at adjacent timesteps along the MD trajectory as[55]

$$H_{ij}(t + \Delta t/2) = -i\hbar \left\langle \Psi_i(t + \Delta t/2) \left| \frac{\partial}{\partial t} \right| \Psi_j(t + \Delta t/2) \right\rangle \approx \frac{-i\hbar}{2\Delta t}[\langle \Psi_i(t)|\Psi_j(t + \Delta t)\rangle - \langle \Psi_i(t + \Delta t)|\Psi_j(t)\rangle] \quad (1)$$

where Ψ_i and Ψ_j are the wave functions of the electronic state i and j at a given time step. We used the CA-NAC code to calculate the scalar NAC values.[56,57]

Mutual information (MI) was used to establish relationships between the structural properties of $Cs_2AgBiBr_6$ and the NA-MD Hamiltonian. Compared to regression approaches, MI represents relationships between pairs of variables in a more generic manner and can capture highly nonlinear correlations.[35] The pairwise MI was calculated based on entropy estimates from k-nearest-neighbor distances ($k = 3$) as[58]

$$I(X, Y) = \int\int dx\, dy\, p(x, y) \log_2\left(\frac{p(x, y)}{p(x)p(y)}\right) \quad (2)$$

where $p(x,y)$ is the joint probability density of variables x and y and $p(x)$ and $p(y)$ are their marginal densities. One of the variables is an electronic energy gap or a NAC, while the other variable is a structural feature. A large MI implies that knowing the value of one variable reduces the uncertainty of the other variable and that their distributions are strongly correlated.

Figure 1a shows the crystal structure of the $Cs_2AgBiBr_6$ double perovskite with the cubic lattice. Br^- interacts with Ag^+ and Bi^{3+} to form octahedral coordination. The octahedra form

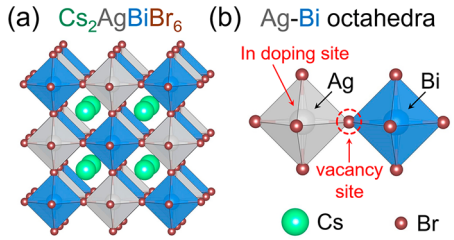

Figure 1. (a) Crystal structure of $Cs_2AgBiBr_6$ double perovskite and (b) local structure of adjacent Ag and Bi octahedra.

a lattice by sharing vertices. Cs^+ is located within the cuboctahedral cavities to support the framework.[9] Figure 1b displays the local structure of the adjacent Ag and Bi octahedra. We introduce V_{Br}^- by removing a Br atom and adding an electron, creating the V_{Br}^- model. Because Ag^+ and Bi^{3+} have the $5s^0$ and $6s^2$ outer electron configurations, respectively, we further replace Ag^+ with In^+ to introduce the $5s^2$ configuration, forming the In-doped V_{Br}^- model. The empty s orbitals are highly delocalized and may rehybridize to trap electrons from the vacancies as reported in the metal oxide systems,[59] while the occupied orbitals can prevent such processes.

MD simulations were performed to investigate structural and electronic behavior of the pristine, defective, and doped $Cs_2AgBiBr_6$ subject to thermal fluctuations at room temperature. Figure 2a displays the time evolution of the conduction band minimum (CBM), the valence band maximum (VBM), and the energy level of the defect-induced trap state in the different models. The CBM and VBM fluctuations are similar in all the models, with the amplitudes and frequencies slightly affected by the defects. In the V_{Br}^- system, an occupied defect state is first introduced near the CBM as a shallow trap, which is consistent with the so-called defect tolerance of perovskites.[60,61] Such trap state is unlikely to accelerate charge carrier recombination, since carriers can escape from it by thermal excitation. However, this shallow state moves downward in energy to become a deep trap after about 2 ps. The results of the In-doped V_{Br}^- system demonstrate that replacing Ag with In prohibits this transition and maintains the trap shallow.

The density of states (DOS) and electron localization function (ELF) were calculated to further clarify these observations, as shown in Figure 2b. The ELF plot of the pristine system illustrates that Br^- prefers to coordinate with Bi^{3+} rather than Ag^+ despite the similar bond lengths in the two cases. After V_{Br}^- is introduced, the adjacent Bi^{3+} first accepts the unbound electrons but places them at a highly localized region. The electrostatic repulsion makes this configuration unstable, and the trap level is therefore as high as the VBM. The Ag^+ atom next to the vacancy approaches Bi^{3+}, shares the accumulated electrons, stabilizes the system, and lowers the energy level of the trap state deep into the bandgap. In comparison, In^+ and Bi^{3+} have similar coordination properties, and thus the charge redistribution and the energy level shift are avoided.

Figure 3 presents distributions of the energy gaps and NACs between CBM, VBM, and the trap state obtained from the MD trajectories. The CBM−VBM bandgaps have similar, Gaussian-like distributions for all the systems with an average value of about 1.6 eV. The shift in the V_{Br}^- defect level gives rise to two peaks in the CBM−trap and trap−VBM energy gap results.

https://doi.org/10.1021/acs.jpclett.2c00869
J. Phys. Chem. Lett. 2022, 13, 3645−3651

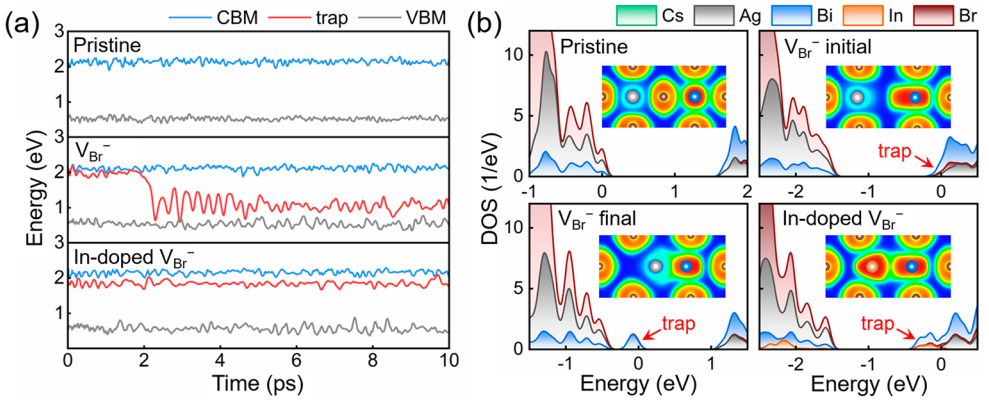

Figure 2. (a) Evolutions of CBM, VBM, and the trap level in pristine and defective $Cs_2AgBiBr_6$ systems during the MD simulations and (b) the element-projected density of states (DOS) results from static calculations. The highest occupied energy level is set to zero. The inset show the electron localization function (ELF) maps around the vacancy sites. Red and blue indicate the ELF values of 1 and 0, respectively. The atom color code is the same as in Figure 1.

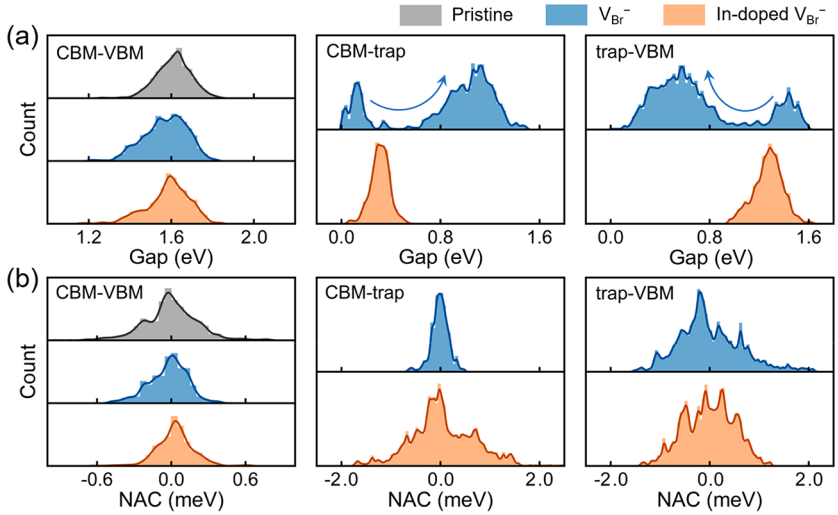

Figure 3. Probability distributions of (a) the energy gap and (b) the NAC between CBM, VBM, and the trap state in different systems. The blue arrows indicate the trap level shift during the MD simulations.

Table 1. Mutual Information of Energy Gaps and NACs with Structural Features[a]

		MI(gap)			MI(NAC)		
model	feature	CBM−VBM	CBM−trap	trap−VBM	CBM−VBM	CBM−trap	trap−VBM
pristine	Δr(Cs)	1.02			1.44		
	∠Br−Br−Br	1.03			1.43		
V_{Br}^-	Δx(Ag*)	1.56	2.95	2.76	1.88	2.11	1.67
	Δx(Bi*)	1.38	2.41	2.35	1.81	2.14	1.64
	d(Ag*−Bi*)	1.36	2.35	2.34	1.56	1.74	1.43
	Δr(Cs)	1.44	2.45	2.34	1.72	1.98	1.56
In-doped V_{Br}^-	Δx(In*)	1.30	1.65	1.51	1.40	1.60	1.51
	Δx(Bi*)	1.46	1.73	1.56	1.70	1.85	1.85
	d(In*−Bi*)	1.14	1.48	1.31	1.38	1.67	1.58
	Δr(Cs)	1.43	1.70	1.59	1.58	1.76	1.82

[a] Δr and Δx are the total displacement and the displacement along the x-axis, respectively. ∠ is the bond angle, and d is the bond length. Ag*, Bi*, and In* are the atoms at the vacancy site. The Bi*−V_{Br}^-−Ag*/In* direction is set as the z-axis.

The energy gaps of the V_{Br}^- system have broader distributions than the others energy gaps, especially after the transition of the defect level deep into the bandgap. This observation implies a significant fluctuation of the defect level energy induced by the charge redistribution between the Ag and Bi ions. The NACs of the last 4 ps of the trajectories were calculated to characterize charge carrier recombination. The small NACs between CBM and VBM indicate that the direct recombination bypassing trapping is unlikely to occur. The NACs between the trap state and either CBM or VBM are notably larger than the CBM−VBM NAC (Figure 3), indicating that the energy and charge losses occur by through

https://doi.org/10.1021/acs.jpclett.2c00869
J. Phys. Chem. Lett. 2022, 13, 3645−3651

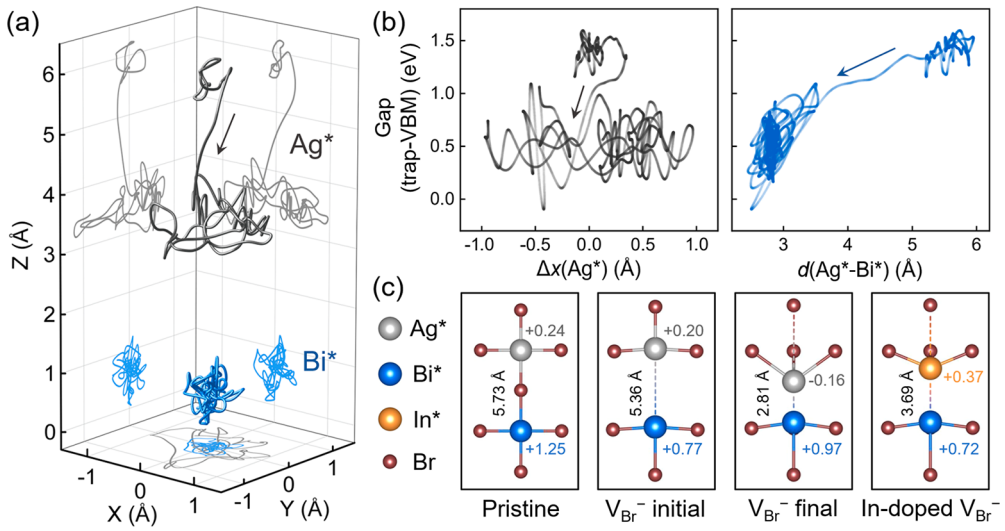

Figure 4. (a) Trajectories of the Ag and Bi atoms at the vacancy site (Ag* and Bi*) in the V_{Br}^- system. The equilibrium position of Bi* in the pristine system is set as the coordinate zero point. (b) Joint distributions of the energy gap between the trap level and VBM with Δx(Ag*) and d(Ag*−Bi*) in the V_{Br}^- system. (c) Local configurations and atomic charge populations around the vacancy sites in different systems.

trapping and that they are notably faster in the defective than pristine system. Although the In dopant prevents the formation of the deep trap, which charge carriers cannot escape, the doped system will still exhibit shorter carrier lifetime than the pristine system.

To identify the key components of the recombination centers produced by the charge redistribution between Ag and Bi, we employed unsupervised ML and established correlations between the electronic properties and the structural features. The atom displacements, bond lengths, bond angles, and distances between unbonded atoms were chosen, and MI between these features and the energy gap or the NAC were calculated (eq 2). The features are illustrated in Figure S1. The MI was averaged over features of the same type. Some important results are shown in Table 1, and the full data can be found in Tables S1−S3. For the pristine system, the Cs displacement (Δr(Cs)) and the Br−Br−Br angle (∠Br−Br−Br) have the highest MI with the bandgap and NAC. The importance of the Cs displacement is somewhat surprising, since Cs does not contribute to any of the electronic states under consideration. Considering that the properties of the Cs atoms are affected little by V_{Br}^-, we use the MI of Δr(Cs) as a benchmark to evaluate if a feature has a significant influence on the electronic properties of the defective systems. Although the trap level shift in the V_{Br}^- system is accompanied by the distinct Ag−Bi distance decrease, surprisingly, we find that this distance, d(Ag*−Bi*), where * refers to the atoms around the vacancy site, has a smaller MI than Δr(Cs) with both the energy gaps and the NACs. Inversely, the displacement of Ag* along the perpendicular direction, Δx(Ag*), has a high MI with the energy gaps. The results indicate that the properties of the trap state are dominated by the charge acceptor Ag* and that even the CBM and VBM are influenced by Ag*. Δx(Ag*) and Δx(Bi*) have high MI with the NAC, suggesting that the charge donor Bi* plays an important role in the carrier recombination. The analysis of the energy gaps and NACs in the V_{Br}^- system reveals that the charge redistribution plays a particular important role in producing the deep recombination center. In addition, only Δx(Bi*) has high MI with the energy gaps and NACs in the In-doped V_{Br}^- system, as the vacancy electrons remain at Bi*, rationalizing the observation.

Performing the unsupervised ML analysis on the NA-MD Hamiltonian, we uncovered that the displacements of the Ag* and Bi* atoms perpendicular to the Ag*−Bi* direction are particularly important during the trap-assisted charge recombination in the defective systems. However, the electronic structure analysis has demonstrated that the trap state originates from the Ag*/In*−V_{Br}^-−Bi* interactions. To clarify such apparent discrepancy, we investigated further relationships between the ion displacements and the energy gap and NAC. Figure 4a shows the trajectories of Ag* and Bi* in the V_{Br}^- system during the MD simulation. Besides the decrease in the Ag*−Bi* distance discussed above, we notice that the movement of Ag* in the x−y plane is greatly enhanced when it approaches Bi*. Figure 4b displays the distribution of the trap−VBM energy gap as a function of Δx(Ag*) and d(Ag*−Bi*) in the V_{Br}^- system. The data points in both plots can be visibly divided into two parts through a transition along the arrows, associated with the Ag* migration. Although the d(Ag*−Bi*) plot exhibits a clearer correlation than the Δx(Ag*) plot, there are many points in the left part with similar d(Ag*−Bi*) values but different energy gaps. From the information perspective, knowing the d(Ag*−Bi*) value in such a distribution can hardly reduce the uncertainty of the energy gap, and thus the MI between these two variables is relatively low (Table S2). In comparison, the points are separated more along the x-axis in the Δx(Ag*) plot, and the energy gap fluctuation can be better represented by the Δx(Ag*) evolution, which implies that these two variables are correlated and the relevant MI is high. It is hard to discern the correlation from the energy gap vs Δx(Ag*) plot (Figure 4b) because the correlation is not linear. The MI function, eq 2, can capture such nonlinear correlation. More results for the V_{Br}^- system are given in Figures S2 and S3. The high MI of Δx(Bi*) in the In-doped V_{Br}^- system can be interpreted similarly, as illustrated in Figures S4 and S5.

Bader charges were calculated to quantitatively study the impact of the charge redistribution, as shown in Figure 4c.[62] Consistent with the DOS results, Bi* is first reduced by the

https://doi.org/10.1021/acs.jpclett.2c00869
J. Phys. Chem. Lett. 2022, 13, 3645−3651

electrons from V_{Br}^{-}, and then, after the Bi*−Ag* distance shortens, Bi* shares the electrons with Ag*. As Ag* gains the excess electrons, it even becomes negatively charged. The reduced Ag* is expected to be repulsed by Br^{-} and bond tightly with Bi* through the electrostatic interaction, which can explain the different distributions of Δx(Ag*) and d(Ag*−Bi*) observed in Figure 4b. The electrons in the In-doped V_{Br}^{-} system are maintained at Bi* despite the interaction between In* and Bi*. The population analysis demonstrates that the charge redistribution significantly influences the coordination of Ag* and magnifies its structural distortion under thermal fluctuations.

In summary, using DFT and applying unsupervised ML to the NA-MD Hamiltonian, we have demonstrated that charge redistribution between the metal atom pair around a Br vacancy is the key factor responsible for the deep charge recombination center in the $Cs_2AgBiBr_6$ double perovskite. The DFT calculations indicate that the electrons from the vacancy are first accepted by the adjacent Bi atom (Bi*) and then are shared with the Ag atom at the vacancy site (Ag*). The charge transfer transforms the trap state from shallow to deep. Although this process is accompanied by migration of Ag* toward Bi*, the ML analysis shows that the key electronic properties, i.e., the energy gaps and NACs, are governed by displacements of Ag* and Bi* perpendicular to the Ag*−Bi* direction. These results highlight the individual roles of the charge donor and acceptor in the carrier recombination rather than their interaction. In addition, replacement of Ag* with In efficiently maintains the vacancy electrons at Bi* and prevents formation of the deep trap. The charge redistribution between Ag* and Bi* not only shifts the trap level but also changes the Ag* coordination. The correlations of the system electronic properties with the particular Ag* motions, as well as with other geometric features, such as Cs displacement and Br−Br−Br angle, are hard to anticipate a priori. In the presence of numerous structural features, the unsupervised ML has allowed us to uncover the most important parameters that govern the charge trapping and recombination. The work has demonstrated that ML is a powerful tool for identifying the key components of charge recombination centers in perovskites and other novel optoelectronic materials and can be used to generate guidelines for defect passivation and development of better perovskite solar cell materials.

■ ASSOCIATED CONTENT

Supporting Information

The Supporting Information is available free of charge at https://pubs.acs.org/doi/10.1021/acs.jpclett.2c00869.

Illustration of the structural features, full data of the mutual information results, joint distributions of the electronic properties with the structural features in the V_{Br}^{-} and In-doped V_{Br}^{-} systems (PDF)

■ AUTHOR INFORMATION

Corresponding Authors

Andrey S. Vasenko − *HSE University, 101000 Moscow, Russia; I.E. Tamm Department of Theoretical Physics, P.N. Lebedev Physical Institute, Russian Academy of Sciences, 119991 Moscow, Russia;* orcid.org/0000-0002-2978-8650; Email: avasenko@hse.ru

Oleg V. Prezhdo − *Department of Chemistry and Department of Physics & Astronomy, University of Southern California, Los Angeles, California 90089, United States;* orcid.org/0000-0002-5140-7500; Email: prezhdo@usc.edu

Authors

Dongyu Liu − *HSE University, 101000 Moscow, Russia;* orcid.org/0000-0001-6941-1885

Carlos Mora Perez − *Department of Chemistry, University of Southern California, Los Angeles, California 90089, United States*

Complete contact information is available at: https://pubs.acs.org/10.1021/acs.jpclett.2c00869

Notes

The authors declare no competing financial interest.

■ ACKNOWLEDGMENTS

The authors are grateful to Prof. Wei Li, Hunan Agricultural University, for fruitful discussions. This research was supported in part through computational resources of HPC facilities at HSE University. A.S.V. acknowledges support from the Basic Research Program of the HSE University. O.V.P. acknowledges support of the USA National Science Foundation, Grant CHE-2154367.

■ REFERENCES

(1) Kim, J. Y.; Lee, J.-W.; Jung, H. S.; Shin, H.; Park, N.-G. High-Efficiency Perovskite Solar Cells. *Chem. Rev.* **2020**, *120*, 7867−7918.

(2) Kojima, A.; Teshima, K.; Shirai, Y.; Miyasaka, T. Organometal Halide Perovskites as Visible-Light Sensitizers for Photovoltaic Cells. *J. Am. Chem. Soc.* **2009**, *131*, 6050−6051.

(3) Kim, G.-H.; Kim, D. S. Development of Perovskite Solar Cells with > 25% Conversion Efficiency. *Joule* **2021**, *5*, 1033−1035.

(4) Kim, M.; Jeong, J.; Lu, H.; Lee, T. K.; Eickemeyer, F. T.; Liu, Y.; Choi, I. W.; Choi, S. J.; Jo, Y.; Kim, H.-B.; et al. Conformal Quantum Dot−SnO_2 Layers as Electron Transporters for Efficient Perovskite Solar Cells. *Science* **2022**, *375*, 302−306.

(5) Xiao, Z.; Song, Z.; Yan, Y. From Lead Halide Perovskites to Lead-Free Metal Halide Perovskites and Perovskite Derivatives. *Adv. Mater.* **2019**, *31*, 1803792.

(6) Chu, W.; Zheng, Q.; Prezhdo, O. V.; Zhao, J.; Saidi, W. A. Low-Frequency Lattice Phonons in Halide Perovskites Explain High Defect Tolerance toward Electron-Hole Recombination. *Sci. Adv.* **2020**, *6*, eaaw7453.

(7) Cao, J.; Yan, F. Recent Progress in Tin-Based Perovskite Solar Cells. *Energy Environ. Sci.* **2021**, *14*, 1286−1325.

(8) Pitaro, M.; Tekelenburg, E. K.; Shao, S.; Loi, M. A. Tin Halide Perovskites: From Fundamental Properties to Solar Cells. *Adv. Mater.* **2022**, *34*, 2105844.

(9) Yang, X.; Wang, W.; Ran, R.; Zhou, W.; Shao, Z. Recent Advances in $Cs_2AgBiBr_6$-Based Halide Double Perovskites as Lead-Free and Inorganic Light Absorbers for Perovskite Solar Cells. *Energy Fuels* **2020**, *34*, 10513−10528.

(10) Lei, H.; Hardy, D.; Gao, F. Lead-Free Double Perovskite $Cs_2AgBiBr_6$: Fundamentals, Applications, and Perspectives. *Adv. Funct. Mater.* **2021**, *31*, 2105898.

(11) She, Y.; Hou, Z.; Prezhdo, O. V.; Li, W. Identifying and Passivating Killer Defects in Pb-Free Double $Cs_2AgBiBr_6$ Perovskite. *J. Phys. Chem. Lett.* **2021**, *12*, 10581−10588.

(12) Hoye, R. L. Z.; Eyre, L.; Wei, F.; Brivio, F.; Sadhanala, A.; Sun, S.; Li, W.; Zhang, K. H. L.; MacManus-Driscoll, J. L.; Bristowe, P. D.; et al. Fundamental Carrier Lifetime Exceeding 1 μs in $Cs_2AgBiBr_6$ Double Perovskite. *Adv. Mater. Interfaces* **2018**, *5*, 1800464.

(13) Delor, M.; Slavney, A. H.; Wolf, N. R.; Filip, M. R.; Neaton, J. B.; Karunadasa, H. I.; Ginsberg, N. S. Carrier Diffusion Lengths Exceeding 1 μm Despite Trap-Limited Transport in Halide Double Perovskites. *ACS Energy Lett.* **2020**, *5*, 1337−1345.

(14) Tress, W.; Sirtl, M. T. $Cs_2AgBiBr_6$ Double Perovskites as Lead-Free Alternatives for Perovskite Solar Cells? *Sol. RRL* **2022**, *6*, 2100770.
(15) Wang, B.; Li, N.; Yang, L.; Dall'Agnese, C.; Jena, A. K.; Sasaki, S.; Miyasaka, T.; Tamiaki, H.; Wang, X.-F. Chlorophyll Derivative-Sensitized TiO_2 Electron Transport Layer for Record Efficiency of $Cs_2AgBiBr_6$ Double Perovskite Solar Cells. *J. Am. Chem. Soc.* **2021**, *143*, 2207−2211.
(16) Wang, B.; Li, N.; Yang, L.; Dall'Agnese, C.; Jena, A. K.; Miyasaka, T.; Wang, X.-F. Organic Dye/$Cs_2AgBiBr_6$ Double Perovskite Heterojunction Solar Cells. *J. Am. Chem. Soc.* **2021**, *143*, 14877−14883.
(17) Sirtl, M. T.; Hooijer, R.; Armer, M.; Ebadi, F. G.; Mohammadi, M.; Maheu, C.; Weis, A.; van Gorkom, B. T.; Häringer, S.; Janssen, R. A. J.; et al. 2D/3D Hybrid $Cs_2AgBiBr_6$ Double Perovskite Solar Cells: Improved Energy Level Alignment for Higher Contact-Selectivity and Large Open Circuit Voltage. *Adv. Energy Mater.* **2022**, *12*, 2103215.
(18) Li, W.; She, Y.; Vasenko, A. S.; Prezhdo, O. V. *Ab Initio* Nonadiabatic Molecular Dynamics of Charge Carriers in Metal Halide Perovskites. *Nanoscale* **2021**, *13*, 10239−10265.
(19) Yang, B.; Chen, J.; Yang, S.; Hong, F.; Sun, L.; Han, P.; Pullerits, T.; Deng, W.; Han, K. Lead-Free Silver-Bismuth Halide Double Perovskite Nanocrystals. *Angew. Chem., Int. Ed.* **2018**, *57*, 5359−5363.
(20) Longo, G.; Mahesh, S.; Buizza, L. R. V.; Wright, A. D.; Ramadan, A. J.; Abdi-Jalebi, M.; Nayak, P. K.; Herz, L. M.; Snaith, H. J. Understanding the Performance-Limiting Factors of $Cs_2AgBiBr_6$ Double-Perovskite Solar Cells. *ACS Energy Lett.* **2020**, *5*, 2200−2207.
(21) Yin, Y.; Tian, W.; Leng, J.; Bian, J.; Jin, S. Carrier Transport Limited by Trap State in $Cs_2AgBiBr_6$ Double Perovskites. *J. Phys. Chem. Lett.* **2020**, *11*, 6956−6963.
(22) Wu, B.; Ning, W.; Xu, Q.; Manjappa, M.; Feng, M.; Ye, S.; Fu, J.; Lie, S.; Yin, T.; Wang, F.; et al. Strong Self-Trapping by Deformation Potential Limits Photovoltaic Performance in Bismuth Double Perovskite. *Sci. Adv.* **2021**, *7*, eabd3160.
(23) Jin, H.; Debroye, E.; Keshavarz, M.; Scheblykin, I. G.; Roeffaers, M. B. J.; Hofkens, J.; Steele, J. A. It's a Trap! On the Nature of Localised States and Charge Trapping in Lead Halide Perovskites. *Mater. Horiz.* **2020**, *7*, 397−410.
(24) Li, X.; Xie, Y.; Hu, D.; Lan, Z. Analysis of the Geometrical Evolution in On-the-Fly Surface-Hopping Nonadiabatic Dynamics with Machine Learning Dimensionality Reduction Approaches: Classical Multidimensional Scaling and Isometric Feature Mapping. *J. Chem. Theory Comput.* **2017**, *13*, 4611−4623.
(25) Tavadze, P.; Avendaño Franco, G.; Ren, P.; Wen, X.; Li, Y.; Lewis, J. P. A Machine-Driven Hunt for Global Reaction Coordinates of Azobenzene Photoisomerization. *J. Am. Chem. Soc.* **2018**, *140*, 285−290.
(26) Dral, P. O.; Barbatti, M.; Thiel, W. Nonadiabatic Excited-State Dynamics with Machine Learning. *J. Phys. Chem. Lett.* **2018**, *9*, 5660−5663.
(27) Westermayr, J.; Gastegger, M.; Marquetand, P. Combining SchNet and SHARC: The SchNarc Machine Learning Approach for Excited-State Dynamics. *J. Phys. Chem. Lett.* **2020**, *11*, 3828−3834.
(28) Bai, X.; Guo, X.; Wang, L. Machine Learning Approach to Calculate Electronic Couplings between Quasi-Diabatic Molecular Orbitals: The Case of DNA. *J. Phys. Chem. Lett.* **2021**, *12*, 10457−10464.
(29) Akimov, A. V. Extending the Time Scales of Nonadiabatic Molecular Dynamics via Machine Learning in the Time Domain. *J. Phys. Chem. Lett.* **2021**, *12*, 12119−12128.
(30) Li, J.; Stein, R.; Adrion, D. M.; Lopez, S. A. Machine-Learning Photodynamics Simulations Uncover the Role of Substituent Effects on the Photochemical Formation of Cubanes. *J. Am. Chem. Soc.* **2021**, *143*, 20166−20175.
(31) Zhang, Z.; Zhang, Y.; Wang, J.; Xu, J.; Long, R. Doping-Induced Charge Localization Suppresses Electron−Hole Recombination in Copper Zinc Tin Sulfide: Quantum Dynamics Combined with Deep Neural Networks Analysis. *J. Phys. Chem. Lett.* **2021**, *12*, 835−842.
(32) Peng, J.; Xie, Y.; Hu, D.; Lan, Z. Analysis of Bath Motion in MM-SQC Dynamics via Dimensionality Reduction Approach: Principal Component Analysis. *J. Chem. Phys.* **2021**, *154*, 094122.
(33) Prezhdo, O. V. Modeling Non-Adiabatic Dynamics in Nanoscale and Condensed Matter Systems. *Acc. Chem. Res.* **2021**, *54*, 4239−4249.
(34) Zhou, G.; Chu, W.; Prezhdo, O. V. Structural Deformation Controls Charge Losses in $MAPbI_3$: Unsupervised Machine Learning of Nonadiabatic Molecular Dynamics. *ACS Energy Lett.* **2020**, *5*, 1930−1938.
(35) Mangan, S. M.; Zhou, G.; Chu, W.; Prezhdo, O. V. Dependence between Structural and Electronic Properties of $CsPbI_3$: Unsupervised Machine Learning of Nonadiabatic Molecular Dynamics. *J. Phys. Chem. Lett.* **2021**, *12*, 8672−8678.
(36) How, W. B.; Wang, B.; Chu, W.; Tkatchenko, A.; Prezhdo, O. V. Significance of the Chemical Environment of an Element in Nonadiabatic Molecular Dynamics: Feature Selection and Dimensionality Reduction with Machine Learning. *J. Phys. Chem. Lett.* **2021**, *12*, 12026−12032.
(37) How, W. B.; Wang, B.; Chu, W.; Kovalenko, S. M.; Tkatchenko, A.; Prezhdo, O. V. Dimensionality Reduction in Machine Learning for Nonadiabatic Molecular Dynamics: Effectiveness of Elemental Sublattices in Lead Halide Perovskites. *J. Chem. Phys.* **2022**, *156*, 054110.
(38) Li, J.-L.; Yang, J.; Wu, T.; Wei, S.-H. Formation of DY Center as n-Type Limiting Defects in Octahedral Semiconductors: The Case of Bi-Doped Hybrid Halide Perovskites. *J. Mater. Chem. C* **2019**, *7*, 4230−4234.
(39) Shi, R.; Fang, W.-H.; Vasenko, A. S.; Long, R.; Prezhdo, O. V. Efficient Passivation of DY Center in $CH_3NH_3PbBr_3$ by Chlorine: Quantum Molecular Dynamics. *Nano Res.* **2022**, *15*, 2112−2122.
(40) Kresse, G.; Hafner, J. *Ab Initio* Molecular Dynamics for Liquid Metals. *Phys. Rev. B* **1993**, *47*, 558−561.
(41) Kresse, G.; Hafner, J. *Ab Initio* Molecular-Dynamics Simulation of the Liquid-Metal-Amorphous-Semiconductor Transition in Germanium. *Phys. Rev. B* **1994**, *49*, 14251−14269.
(42) Kresse, G.; Furthmüller, J. Efficiency of Ab-Initio Total Energy Calculations for Metals and Semiconductors Using a Plane-Wave Basis Set. *Comput. Mater. Sci.* **1996**, *6*, 15−50.
(43) Kresse, G.; Furthmüller, J. Efficient Iterative Schemes for *Ab Initio* Total-Energy Calculations Using a Plane-Wave Basis Set. *Phys. Rev. B* **1996**, *54*, 11169−11186.
(44) Perdew, J. P.; Burke, K.; Ernzerhof, M. Generalized Gradient Approximation Made Simple. *Phys. Rev. Lett.* **1996**, *77*, 3865−3868.
(45) Blöchl, P. E. Projector Augmented-Wave Method. *Phys. Rev. B* **1994**, *50*, 17953−17979.
(46) Kresse, G.; Joubert, D. From Ultrasoft Pseudopotentials to the Projector Augmented-Wave Method. *Phys. Rev. B* **1999**, *59*, 1758−1775.
(47) Momma, K.; Izumi, F. VESTA 3 for Three-Dimensional Visualization of Crystal, Volumetric and Morphology Data. *J. Appl. Crystallogr.* **2011**, *44*, 1272−1276.
(48) Akimov, A. V.; Prezhdo, O. V. The PYXAID Program for Non-Adiabatic Molecular Dynamics in Condensed Matter Systems. *J. Chem. Theory Comput.* **2013**, *9*, 4959−4972.
(49) Pal, S.; Trivedi, D. J.; Akimov, A. V.; Aradi, B.; Frauenheim, T.; Prezhdo, O. V. Nonadiabatic Molecular Dynamics for Thousand Atom Systems: A Tight-Binding Approach toward PYXAID. *J. Chem. Theory Comput.* **2016**, *12*, 1436−1448.
(50) Gumber, S.; Agrawal, S.; Prezhdo, O. V. Excited State Dynamics in Dual-Defects Modified Graphitic Carbon Nitride. *J. Phys. Chem. Lett.* **2022**, *13*, 1033−1041.
(51) Zhou, Z.; Liu, J.; Long, R.; Li, L.; Guo, L.; Prezhdo, O. V. Control of Charge Carriers Trapping and Relaxation in Hematite by Oxygen Vacancy Charge: *Ab Initio* Non-Adiabatic Molecular Dynamics. *J. Am. Chem. Soc.* **2017**, *139*, 6707−6717.

https://doi.org/10.1021/acs.jpclett.2c00869
J. Phys. Chem. Lett. 2022, 13, 3645−3651

(52) Akimov, A. V.; Asahi, R.; Jinnouchi, R.; Prezhdo, O. V. What Makes the Photocatalytic CO_2 Reduction on N-Doped Ta_2O_5 Efficient: Insights from Nonadiabatic Molecular Dynamics. *J. Am. Chem. Soc.* **2015**, *137*, 11517−11525.
(53) Stier, W.; Duncan, W. R.; Prezhdo, O. V. Thermally Assisted Sub-10 Fs Electron Transfer in Dye-Sensitized Nanocrystalline TiO_2 Solar Cells. *Adv. Mater.* **2004**, *16*, 240−244.
(54) He, J.; Vasenko, A. S.; Long, R.; Prezhdo, O. V. Halide Composition Controls Electron−Hole Recombination in Cesium−Lead Halide Perovskite Quantum Dots: A Time Domain Ab Initio Study. *J. Phys. Chem. Lett.* **2018**, *9*, 1872−1879.
(55) Hammes-Schiffer, S.; Tully, J. C. Proton Transfer in Solution: Molecular Dynamics with Quantum Transitions. *J. Chem. Phys.* **1994**, *101*, 4657−4667.
(56) Chu, W.; Prezhdo, O. V. Concentric Approximation for Fast and Accurate Numerical Evaluation of Nonadiabatic Coupling with Projector Augmented-Wave Pseudopotentials. *J. Phys. Chem. Lett.* **2021**, *12*, 3082−3089.
(57) Chu, W.; Zheng, Q.; Akimov, A. V.; Zhao, J.; Saidi, W. A.; Prezhdo, O. V. Accurate Computation of Nonadiabatic Coupling with Projector Augmented-Wave Pseudopotentials. *J. Phys. Chem. Lett.* **2020**, *11*, 10073−10080.
(58) Kraskov, A.; Stögbauer, H.; Grassberger, P. Estimating Mutual Information. *Phys. Rev. E* **2004**, *69*, 066138.
(59) Buckeridge, J.; Catlow, C. R. A.; Farrow, M. R.; Logsdail, A. J.; Scanlon, D. O.; Keal, T. W.; Sherwood, P.; Woodley, S. M.; Sokol, A. A.; Walsh, A. Deep vs Shallow Nature of Oxygen Vacancies and Consequent n-Type Carrier Concentrations in Transparent Conducting Oxides. *Phys. Rev. Mater.* **2018**, *2*, 054604.
(60) Shi, R.; Vasenko, A. S.; Long, R.; Prezhdo, O. V. Edge Influence on Charge Carrier Localization and Lifetime in $CH_3NH_3PbBr_3$ Perovskite: *Ab Initio* Quantum Dynamics Simulation. *J. Phys. Chem. Lett.* **2020**, *11*, 9100−9109.
(61) Wu, Y.; Chu, W.; Vasenko, A. S.; Prezhdo, O. V. Common Defects Accelerate Charge Carrier Recombination in $CsSnI_3$ without Creating Mid-Gap States. *J. Phys. Chem. Lett.* **2021**, *12*, 8699−8705.
(62) Tang, W.; Sanville, E.; Henkelman, G. A Grid-Based Bader Analysis Algorithm without Lattice Bias. *J. Phys.: Condens. Matter* **2009**, *21*, 084204.

https://doi.org/10.1021/acs.jpclett.2c00869
J. Phys. Chem. Lett. 2022, 13, 3645−3651